Additive Manufacturing 37 (2021) 101650

Contents lists available at ScienceDirect

Additive Manufacturing

journal homepage: www.elsevier.com/locate/addma

An adaptive Finite Element strategy for the numerical simulation of additive manufacturing processes

Joan Baiges [a], Michele Chiumenti [a,b], Carlos A. Moreira [a,b], Miguel Cervera [a,b], Ramon Codina [a,b]

[a] Universitat Politécnica de Catalunya, Jordi Girona 1-3, Edifici C1, 08034 Barcelona, Spain
[b] Centre Internacional de Métodes Numérics a l'Enginyeria (CIMNE), Edifici C1, Campus Nord UPC C/ Gran Capitá S/N, 08034 Barcelona, Spain

ARTICLE INFO

Keywords:
Finite Element
adaptive refinement
additive manufacturing
numerical simulation

ABSTRACT

In this work an adaptive Finite Element strategy to deal with the numerical simulation of Additive Manufacturing (AM) processes is presented. The Selective Laser Melting (SLM) is chosen as the reference technology because of its great diffusion in the industrial manufacturing chain, although the proposed methodology can be applied to the numerical simulation of all types of AM. An octree-based mesh adaptivity approach is adopted allowing for the use of much finer meshes within the processing zone, the so called Thermo-Mechanically Affected Zone (TMAZ), if compared to the rest of the computational domain. Although the adaptive meshing is vital to keep controlled the computational resources through the entire simulation of the fabrication process, the accuracy of the results can be compromised by the coarsening strategy, and particularly when simulating the SLM process, where the mesh size can vary from microns (TMAZ) to centimetres (close to the build-plate). This loss of accuracy can spoil the original efforts in refining the mesh in the process zone. Therefore a strategy to compensate for information loss in the adaptive refinement simulation of additive manufacturing processes is developed. The main idea is to add two correction terms which compensate for the loss of accuracy in the coarsening process of the mesh in the already manufactured regions. The proposed correction terms can be interpreted as a Variational Multiscale enhancement on the adaptive mesh. This allows one to successfully simulate the additive manufacturing process by using an adaptively coarsened mesh, with results which have an accuracy very similar to the one of a uniformly refined mesh simulation, at a fraction of the computational cost. Numerical examples illustrate the performance of the proposed strategy.

1. Introduction

The numerical simulation of Additive Manufacturing (AM) processes has been capturing the interest of the scientific community during the last years. Many efforts have been done to reproduce the fabrication process in a way as faithful as possible to the industrial practice. We refer to *high fidelity* analysis when the objective is to simulate the actual scanning sequence (laser Electron Beam (EB) melting processes) or the metal deposition pattern (wire melting or blown-powder processes). Following this concept, fully coupled thermo-mechanical analysis are conducted on an evolving (growing) computational domain which closely follows the building process.Most of the original works on AM simulation make use of the numerical framework used for the welding or multi-pass welding analysis, adopting very similar numerical strategies to solve the thermal/coupled thermo-mechanical problem [10,13]. These strategies have been applied to validate additive manufacturing numerical simulation using experimental data [16,17,37], including stress and deformation evaluation [32–34]. A review of the residual stresses can be found in [8] and the influence of the how scanning strategies affect the residual stresses are subject of [12,40]. While the constitutive models used for the characterization of the material behavior have demonstrated to be suitable for the AM analysis, the numerical strategy has shown its limitations when trying to afford simulations on components of industrial interest. This problem is more and more evident when moving the focus from Wire Arc Additive Manufacturing (WAAM), where the thickness of the deposited layer is within the range of 1–3 mm, to Selective Laser Melting (SLM), that makes use of a laser source to (selectively) melt powder-bed layers of about 20–60 μm. This is the reason why the numerical simulation of the SLM process is generally addressed using simplified strategies based on the *Inherent Strain* method [11,22,44,48,49]. Hence, the coupled thermo-mechanical process is replaced by a sequence of purely mechanical computations in a layer-by-layer (or even multi-layer) manner. This is physically motivated by the fact that during the recoating

E-mail address: joan.baiges@upc.edu (J. Baiges).

https://doi.org/10.1016/j.addma.2020.101650
Received 17 June 2020; Received in revised form 4 September 2020; Accepted 5 October 2020
Available online 9 October 2020

process, when a new powder-bed is spread, the temperature of the built decreases to reach the value of the build-plate, de-coupling the analysis of the last printed layer from the rest of the built. In the common practice, the Thermo-Mechanically Affected Zone (TMAZ) penetrates only 100–150 μm (just few layers) through the substrate (or the more recent printed layers). Hence, the temperature gradients (induced by the laser source), as well as the evolution of the plastic strains (due to the material shrinkage), affect the last few printed layers, only. A second simplification hypothesis consists of assuming a purely elastic stress analysis being the end-user the final responsible of defining or obtaining a suitable Inherent-Strain tensor that characterizes the process in terms of distortions and residual stresses of the manufactured component. The Inherent-Strain tensor can be obtained from experimental data or previous small-scale, non-linear, numerical simulations [9]. This tensor includes both the thermal and the plastic strains defined as a uniform (averaged) distribution over each printed layer. This hypothesis relays on the fact that the melt-pool is very small, if compared with the size of the entire layer, its effects being very localized and almost independent of the boundary conditions. Other approaches to obtain the Inherent Strain tensor are possible, such as the modified version of the Inherent Strain Method is presented for the Direct Energy Deposition (DED) in LENS (Laser Engineered Net Shaping) presented in [28,29] and the extension of this work for lattice support structures in powder bed technology is introduced in [30].

Although the inherent strain method alleviates the computation requirements for the simulation of the SLM process, the huge number of layers necessary to build the final component as well as the mesh size required for the Finite Element (FE) discretization still need very large computational time and memory requirements.

The approach followed in this work consists in combining a FE High Performance Computing (HPC) framework together with dynamic mesh adaptation, which mitigates the computational effort by refining the mesh at the TMAZ while coarsening it anywhere else. An octree-based coarsening strategy is adopted (see Fig. 1). The main idea of octree strategies is to hierarchically refine/coarsen elements, which allows the refinement process to be efficient and relatively simple to parallelize [18,36,39,41]. The octree method allows for a fast coarsening of the mesh while minimizing the data-transfer between meshes. It also demonstrates to be suitable for its parallelization in MPI-based HPC environments. The enhancement provided by AMR and parallelism for the solution of AM processes can be found in several works.

Ref. [20] uses a coarsening algorithm to reduce the computational cost. The algorithm keeps a fine mesh on the two layers below the deposition area and merges the elements below this region maintaining at least 1 fine layer below the deposition. Plastic strains and hardening variables are interpolated to the new Gauss points. [38] proposes an adaptive re-meshing to minimize the number of nodes to predict distortions and residual stresses in the simulation of LPBF where the layers being solved are kept with a fine mesh and a coarse mesh at the inactive and previous solved layers. [26] uses dynamically changing meshes based on a combination of hp-finite elements and the finite cell method to treat state and field variables to reduce the number of nodes on the simulation to save computational resources.

In [21] a thermo-mechanical LPBF is validated by comparing predicted and measured distortions. The work is based on a multi-scale approach and uses mesh adaptivity to reduce mesh density according to a pre-activation remeshing scheme. The authors refer to the adaptivity as one of the sources of error between the observed results of model-experiment. [27] addresses several coarsening strategies using Hex8 elements with smooth transitions between coarse and fine mesh regions. The authors compare the coarsening strategies with static mesh results validated experimentally comparing temperature field, distortions and residual stresses in a thin wall structure. A common strategy is to apply a dynamic mesh with a refined area near the heat source in LPBF and compare the adaptive solution with a fix uniform mesh for the thermal problem [25,50]. The work of [42] compares the performance of the thermo-mechanical solution using the monolithic and adiabatic [2] approaches using AMR to refine and coarsen structured meshes where required.

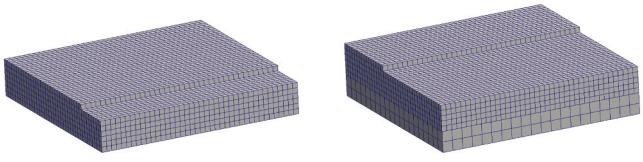

Fig. 1. AM process simulation: Initial uniform mesh (left); mesh coarsening far from the TMAZ (right).

Nevertheless, by using intensive adaptive refinement for the AM processes, one of the main concerns is the loss of information in the data-transfer when switching from a fine mesh (TMAZ) to a coarser one. This information loss can lead to a reduction of accuracy spoiling the final results.

In this work a strategy to compensate for information loss in the adaptive refinement simulation of AM processes is presented. The main idea is to add two correction terms to the boundary value problem defined for the coarser mesh to preserve the results obtained in the finer mesh just before the coarsening procedure. The proposed methodology can be understood as a Variational Multiscale approach [23], in which the model for the subscales arising from finer discretizations is exactly known. The method is derived from the approaches presented in [5,6], where coarsening correction terms were applied in order to enhance the performance of reduced order models.

The proposed correction method is applied to the numerical simulation of SLM processes by the *inherent strain* method. Nevertheless, the same methodology can be extended to the high-fidelity analysis of more complex AM processes (e.g. WAAM, DED, etc.) involving thermo-mechanical coupling and elasto-visco-plastic constitutive behavior.

The paper is organized as follows: in Section 2 the FE modeling of the AM process by SLM is presented. Section 3 focuses on the proposed adaptive methodology and the strategy to correct the information loss in the coarsening process. In Section 4 several numerical examples illustrate the performance of the proposed strategy, and finally some conclusions close the work in Section 5.

2. Finite Element modeling of the additive manufacturing process by SLM

The most suitable numerical strategy to tackle the simulation of the SLM process is based on the Inherent Strain approach. This method enables for a fast prediction of the distortions and residual stresses of the fabricated component assuming the general hypotheses widely accepted in Computational Welding Mechanics (CWM) [35,46,47]. In this case, the fully coupled transient thermo-mechanical analysis is replaced by a layer-by-layer (or even multi-layer) sequence of steady-state mechanical analyses. Hence, the original CAD geometry is firstly sliced according to the thickness of the powder-bed and then the FE discretization is generated accordingly. The birth-death FE activation technique is adopted [14,15,17,19,31] to add to the computational domain Ω all the finite elements belonging to each layer (slice) arising from the laser melting process of the powder bed. The analysis follows the two-step sequence of the actual SLM process: (i) recoating and (ii) laser-scanning. From the modeling point of view, the former consists of updating the computational domain by adding all the elements belonging to each new layer. The latter stage performs the stress analysis on the new domain.

In the initial FE discretization $\Omega_h^o = \Omega_h(t=0)$ all the elements are inactive: they do not belong to the computational domain, so that they are neither computed nor assembled into the global system of equations. The time discretization consists of a uniform partition of the analysis period $[0, T]$ into N time intervals, which correspond to the total number

of layers required to complete the whole SLM process. This given, when the first layer is activated, the corresponding stress analysis is performed on Ω_h^1. The whole layer activation sequence follows.

The stress analysis enforces the conservation of the balance of momentum equation within the current active domain Ω_h^{n+1} at time $t^{n+1} \in [0, T]$. We denote as t^{n+1} the current time instant to indicate that an implicit approach for the time integration is used. The corresponding Dirichlet and Neumann boundary conditions are applied on $\Gamma_D^{n+1} = \Gamma_D(t^{n+1})$ and $\Gamma_N^{n+1} = \Gamma_N(t^{n+1})$, respectively, which results in the following set of equations:

$$\begin{aligned} -\nabla\cdot\boldsymbol{\sigma} &= b \quad \text{in } \Omega_h^{n+1}, \\ u &= \bar{u} \quad \text{on } \Gamma_D^{n+1}, \\ \boldsymbol{\sigma}\cdot n &= \bar{t} \quad \text{on } \Gamma_N^{n+1}, \end{aligned} \tag{1}$$

where $\boldsymbol{u}$ is the displacement field, $\boldsymbol{\sigma}$ is the Cauchy stress tensor, $\boldsymbol{b}$ are the external body forces and, $\bar{\boldsymbol{u}}$ and $\bar{\boldsymbol{t}}$ are the prescribed displacements and the prescribed tractions on Γ_D^{n+1} and Γ_N^{n+1}, respectively.

After the finite element discretization, the discrete weak form of (1) at time $t^{n+1} \in [0, T]$ can be written as:

$$\begin{aligned} \int_{\Omega_h^{n+1}} \boldsymbol{\epsilon}(\delta\boldsymbol{v}_h) : \boldsymbol{\sigma}(\boldsymbol{u}_h^{n+1})\, d\Omega &= \int_{\Omega_h^{n+1}} \delta\boldsymbol{v}_h\cdot\boldsymbol{b}\, d\Omega \\ &+ \int_{\Gamma_N^{n+1}} \delta\boldsymbol{v}_h\cdot\bar{\boldsymbol{t}}\, d\Gamma \quad \forall\delta\boldsymbol{v}_h \in V_h^{n+1}. \end{aligned} \tag{2}$$

where $\delta\boldsymbol{v}_h$ are the test functions and V_h^{n+1} is the finite element space for the displacements.

The total strain tensor $\boldsymbol{\epsilon}(\boldsymbol{u}) = \frac{1}{2}\left(\nabla\boldsymbol{u} + (\nabla\boldsymbol{u})^T\right) = \nabla^S\boldsymbol{u}$ can be split into the elastic strains, $\boldsymbol{\epsilon}_e$, the visco-plastic strains including phase transformation and creep induced strains, $\boldsymbol{\epsilon}_{vp}$, and the thermal deformation including the shrinkage effect during the phase-change transformation, $\boldsymbol{\epsilon}_{th}$, as:

$$\epsilon = \epsilon_e + \epsilon_{vp} + \epsilon_{th} \tag{3}$$

The constitutive model reads as:

$$\boldsymbol{\sigma} = \mathbb{C} : \boldsymbol{\epsilon}_e = \mathbb{C} : \left(\boldsymbol{\epsilon} - \boldsymbol{\epsilon}_{vp} - \boldsymbol{\epsilon}_{th}\right) \tag{4}$$

where $\mathbb{C}$ is the elastic constitutive tensor. Defining the inherent strain as: $\boldsymbol{\epsilon}_{inh} = \boldsymbol{\epsilon}_{vp} + \boldsymbol{\epsilon}_{th}$, the constitutive equation can be rewritten as:

$$\boldsymbol{\sigma}(\boldsymbol{u}) = \mathbb{C} : (\boldsymbol{\epsilon}(\boldsymbol{u}) - \boldsymbol{\epsilon}_{inh}) \tag{5}$$

Note that the inherent strain tensor is typically obtained either by experimental calibration by matching the actual distortion of representative demonstrators or by a high-fidelity simulation of the moving melt-pool at the TMAZ [24,43,45]. Hence, both the thermal coupling and the plastic analysis are avoided, thus minimizing the computational cost.

Nevertheless, according to the activation process, each new layer is born with an initial displacement field, $\boldsymbol{u}_o$, induced by the movement of the nodes shared with the pre-existing active elements. This means that at the instant of the activation, the newly activated elements inherit an initial strain field $\boldsymbol{\epsilon}(\boldsymbol{u}_o) = \nabla^S\boldsymbol{u}_o$ induced by those initial displacements. If not removed from the computation, this strains transform into a spurious pre-stress field which pollutes the entire solution. Hence, to deal with the AM analysis, the constitutive equation must be corrected as:

$$\boldsymbol{\sigma}(\boldsymbol{u}, \boldsymbol{\epsilon}_{inh}, \boldsymbol{\epsilon}_{act}) = \mathbb{C} : (\boldsymbol{\epsilon}(\boldsymbol{u}) - \boldsymbol{\epsilon}_{inh} - \boldsymbol{\epsilon}_{act}) \tag{6}$$

where $\boldsymbol{\epsilon}_{act} = \nabla^S\boldsymbol{u}_o$ are the so called activation strains.

Fig. 2 illustrates the displacement field caused by the effect of the inherent strains $\boldsymbol{\epsilon}_{inh}$. Displacements are magnified by several orders of magnitude so that they can be appreciated in the figure. Active elements are depicted in red, while inactive elements are depicted in green. The highlighted green element is the element which is going to be activated in the next time step. The element is deformed due to the displacements of the nodes which belong to already activated elements. This initial or activation deformation shall not introduce any stresses in the newly printed material. To compensate for it, the initial or activation strain $\boldsymbol{\epsilon}_{act}$ is introduced.

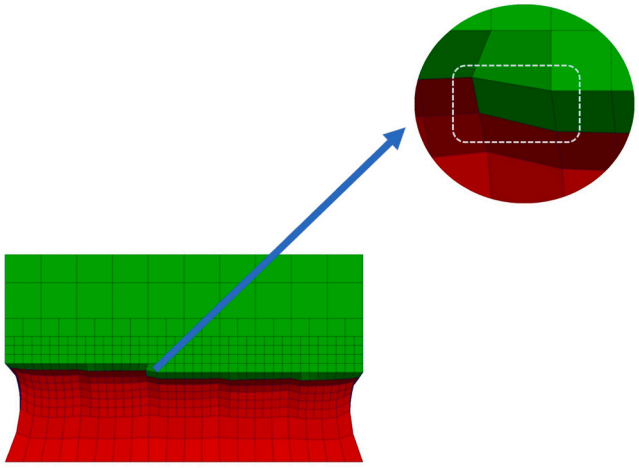

Fig. 2. Displacement field caused by inherent strains.

This given, the weak form of the mechanical problem suitable for AM analysis can be rewritten using the following compact form: find a displacement field $\boldsymbol{u}_h^{n+1}$ such that:

$$B^{n+1}\left(\delta\boldsymbol{v}_h, \boldsymbol{\sigma}(\boldsymbol{u}_h^{n+1}, \epsilon_{act}^{n+1}, \epsilon_{inh}^{n+1})\right) = F^{n+1}(\delta\boldsymbol{v}_h) \quad \forall\delta\boldsymbol{v}_h \in V_h^{n+1}, \tag{7}$$

where

$$\begin{aligned} B^{n+1}\left(\delta\boldsymbol{v}_h, \boldsymbol{\sigma}(\boldsymbol{u}_h^{n+1}, \epsilon_{\text{act}}^{n+1}, \epsilon_{\text{inh}}^{n+1})\right) &:= \int_{\Omega_h^{n+1}} \epsilon(\delta\boldsymbol{v}_h) : \mathbb{C} : \left(\epsilon(\boldsymbol{u}_h^{n+1})\right. \\ &\left. - \epsilon_{\text{act}}^{n+1} - \epsilon_{\text{inh}}^{n+1}\right) d\Omega, \end{aligned} \tag{8}$$

$$F^{n+1}(\delta\boldsymbol{v}_h) := \int_{\Omega_h^{n+1}} \delta\boldsymbol{v}_h\cdot\boldsymbol{b}\, d\Omega + \int_{\Gamma_N^{n+1}} \delta\boldsymbol{v}_h\cdot\bar{\boldsymbol{t}}\, d\Gamma \tag{9}$$

3. Coarsening and correction strategy

3.1. Octree refinement strategy

For the solution of Eq. (7) an adaptive finite element method is used. This is very convenient since it allows to use a fine mesh in the regions where material is being printed and where both large temperature gradients and stress concentrations occur. At the same time it allows to coarsen the mesh once the simulation advances and less precision is required on that area. An octree refinement strategy is used (see our previous works on adaptive methods for computational solid mechanics [3,4,7]). Fig. 1 illustrates the adopted refinement strategy. The simulation departs from a coarse mesh which covers the complete simulation domain over time. The mesh is then refined by subdividing the elements in the areas close to the melt-pool. This can be done for both hexahedral and tetrahedral elements. As the manufacturing process advances, a finer mesh is used in the TMAZ (upper layers), while a mesh coarsening is performed elsewhere. The hierarchical octree refinement strategy results in hanging nodes (see Fig. 3) in the finite element mesh which need to be properly treated [3].

3.2. Adaptive finite element approach

Let us consider an adaptively refined finite element space in the active domain, V_h^{n+1}, and the discrete weak form of the problem given by

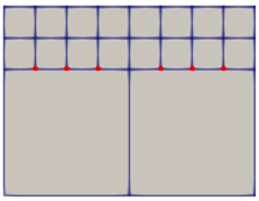

Fig. 3. Hanging nodes (*red*) at the interface between refined and coarse meshes. (For interpretation of the references to color in this figure legend, the reader is referred to the web version of this article.)

Eqs. (7)–(9). Note that the finite element space V_h^{n+1} evolves after the deposition of each new layer following the printing process, as well because of the adaptive refinement and coarsening process. When a new finite element mesh is generated because of the mesh adaptivity process, information from the previous mesh needs to be projected onto the new mesh.

For the displacement field, a nodal projection is used, which means that for already existing nodes the nodal displacement values do not change, and for new nodes, the values are interpolated point to point from the old mesh onto the new one. Therefore, the displacements at t^n in the mesh at t^{n+1} are given by:

$$P_h^{n+1}\left(\boldsymbol{u}_h^n\right), \tag{10}$$

where $P_h^{n+1}(\cdot)$ is the point to point projection onto V_h^{n+1}.

For the historical variables defined at the integration points, such as $\boldsymbol{\epsilon}_{act}$ and $\boldsymbol{\epsilon}_{\text{inh}}$, the projection process is done element by element, the quantities are transferred through an elementwise L^2 projection, which is denoted by Π_h^{n+1}. Thus:

$$\Pi_h^{n+1}(\epsilon_{\text{act}}^n), \tag{11}$$

$$\Pi_h^{n+1}(\epsilon_{\text{inh}}^n). \tag{12}$$

are the strains $\boldsymbol{\epsilon}_{\text{act}}$ and $\boldsymbol{\epsilon}_{inh}$ at t^n in the mesh at t^{n+1}. For each element K^{n+1} of the new mesh the projection is computed solving:

$$\int_{K^{n+1}} \delta\boldsymbol{\gamma}_h : \Pi_h^{n+1}(\epsilon^n) d\Omega = \int_{K^{n+1}} \delta\boldsymbol{\gamma}_h : \epsilon^n d\Omega, \quad \forall \delta\boldsymbol{\gamma}_h \in W_{h,K^{n+1}}$$

where now $\delta\boldsymbol{\gamma}_h$ are the tensorial weight functions and $W_{h,K^{n+1}}$ is the tensorial finite element space of the new mesh restricted to the considered element. Once computed, $\Pi_h^{n+1}(\boldsymbol{\epsilon}^n)$ is interpolated and stored at the new element quadrature points. Note that $\Pi_h^{n+1}(\boldsymbol{\epsilon}^n)$ belongs to the element-wise tensorial finite element space $W_{h,K^{n+1}}$, which is of the same approximation order as the displacement space V_h^{n+1}, whereas $\boldsymbol{\epsilon}^n$ belongs to the strains finite element space, which is typically one approximation order inferior than the displacement space V_h^{n+1}.

3.3. Stress correction terms

During the coarsening step between successive adaptive meshes, part of the information stored in the coarsened region is lost. This is so because of the projection errors associated to P_h^{n+1} and Π_h^{n+1}, and also because in the coarsening process the finite element space changes from V_h^n to V_h^{n+1}. This causes that when straightforwardly computing the stresses which result from the adaptive simulation of the AM process by using inherent and activation strains, it is observed that the obtained results are of poor quality and not in concordance with those obtained with an equivalent fine mesh simulation. This effect is particularly apparent when low order elements with a poor representation of the stress field (namely tetrahedral elements) are used. The obtained stress field if of a much lower quality than the one obtained for coarser non-adaptive meshes.

The reason for this behavior is twofold: on the one hand the activation (or inherent) strains on the fine mesh before coarsening $\boldsymbol{\epsilon}_{act}^n$ can present heavy element to element jumps, specially if low order elements with a poor gradient representation are used. When coarsened, activation strains result in an L^2 averaged field $\Pi_h^{n+1}(\boldsymbol{\epsilon}_{act}^n)$ which introduces the appropriate average forces field, but which can result in an inaccurate local strain value. This representation is translated into a poor local solution stress field when the next step of the simulation is performed. Secondly, when mesh coarsening is performed, there will be nodes which were previously free which will become hanging in the new mesh. Displacement values at these nodes will automatically be switched from their free value to an interpolated value from the corresponding parent nodes. This results in important changes in the strain values, which automatically translates into incorrect local stress values on the elements to which these hanging nodes belong.

Due to this, it is necessary to correct the obtained stress values through a stress correction term. Let us define the stress field on the current step $\boldsymbol{\sigma}_h^{n+1}$ straightforwardly computed from the current step variables:

$$\boldsymbol{\sigma}_h^{n+1} = \boldsymbol{\sigma}\left(\boldsymbol{u}_h^{n+1}, \epsilon_{act}^{n+1}, \epsilon_{inh}^{n+1}\right), \tag{13}$$

and the stresses from the previous time step computed on the current step mesh, by using the projected previous step variables, $\hat{\boldsymbol{\sigma}}_h^n$:

$$\hat{\boldsymbol{\sigma}}_h^n = \boldsymbol{\sigma}\left(P_h^{n+1}(\boldsymbol{u}_h^n), \Pi_h^{n+1}(\epsilon_{act}^n), \Pi_h^{n+1}(\epsilon_{inh}^n)\right). \tag{14}$$

Note that both quantities are defined in the mesh at step $n+1$. Recall that due to the nature of activation and inherent strains:

$$\begin{aligned} \epsilon_{act}^{n+1} &= \Pi_h^{n+1}(\epsilon_{act}^n) + \Delta\epsilon_{act}^{n+1}, \\ \epsilon_{inh}^{n+1} &= \Pi_h^{n+1}(\epsilon_{inh}^n) + \Delta\epsilon_{inh}^{n+1}. \end{aligned}$$

The proposed total corrected stress field $\boldsymbol{\sigma}^{n+1}$ is defined as:

$$\boldsymbol{\sigma}^{n+1} = \boldsymbol{\sigma}_h^{n+1} + \widetilde{\boldsymbol{\sigma}}^{n+1} \tag{15}$$

with:

$$\widetilde{\boldsymbol{\sigma}}^{n+1} = \Pi_h^{n+1}(\boldsymbol{\sigma}^n) - \hat{\boldsymbol{\sigma}}_h^n, \tag{16}$$

where $\widetilde{\boldsymbol{\sigma}}^{n+1}$ is the stress correction term. Let us remark the recursive nature of Eqs. (15)–(16), where the total corrected stress field $\boldsymbol{\sigma}^{n+1}$ depends on the projection of the total corrected stress field at the previous step $\Pi_h^{n+1}(\boldsymbol{\sigma}^n)$. At the first step $\widetilde{\boldsymbol{\sigma}}^1 = \boldsymbol{0}$ is set. Note also that Eqs. (15)–(16) imply that the total stress at time step $n+1$ can be interpreted as the decomposition into:

$$\boldsymbol{\sigma}^{n+1} = \Pi_h^{n+1}(\boldsymbol{\sigma}^n) + \Delta\boldsymbol{\sigma}^{n+1},$$

where the first term is the contribution of the previous time steps with minimum information loss as a result of the stress correction term, and the second one is the increment in stresses caused by load increments $\Delta\boldsymbol{\epsilon}_{act}^{n+1}$, $\Delta\boldsymbol{\epsilon}_{inh}^{n+1}$ at the current step, with:

$$\Delta\boldsymbol{\sigma}^{n+1} = \boldsymbol{\sigma}_h^{n+1} - \hat{\boldsymbol{\sigma}}_h^n,$$

as defined in Eqs. (13)–(14).

In the first coarsening step, the correction term (16) is just the difference between the projected stress field at the previous time step, and the stress computed in the new mesh with the projected variables from the previous step, namely displacements and inherent and activation strains field. For successive steps, due to the recursive nature of $\widetilde{\boldsymbol{\sigma}}$, information on the fine meshes at previous steps is successively transferred throughout the simulation, minimizing information loss.

3.4. Force correction terms

The introduction of the stress correction terms (16) is not enough to prevent information loss during successive coarsening steps. This is so because there is no guarantee that the solution of the finite element problem in the previous mesh is at equilibrium when projected onto the new coarsened mesh. The optimal situation would be to preserve the results obtained through the solution of problem (7) at time step n into the new (coarsened) finite element mesh at time $n+1$. In general this does not happen and thus:

$$\exists \delta \boldsymbol{v}_h \in \hat{V}_h^{n+1} | B^n\left(\delta \boldsymbol{v}_h, \hat{\boldsymbol{\sigma}}_h^n + \widetilde{\boldsymbol{\sigma}}^{n+1}\right) = B^n\left(\delta \boldsymbol{v}_h, \Pi_h^{n+1}(\boldsymbol{\sigma}^n)\right) \neq F^n(\delta \boldsymbol{v}_h). \tag{17}$$

where now $\hat{V}_h^{n+1}$ is the coarsened finite element space at t^{n+1} prior to the new element activation, that is, the space associated to the mesh at $n+1$ but covering only the domain Ω^n, instead of Ω^{n+1}. Due to this, the equilibrium state *attimestepn* on the coarsened mesh $n+1$ is not attained for $P_h^{n+1}(\boldsymbol{u}_h^n)$ but for $\hat{\boldsymbol{u}}_h^n$, the solution to:

$$B^n\left(\delta \boldsymbol{v}_h, \boldsymbol{\sigma}\left(\hat{\boldsymbol{u}}_h^n, \Pi_h^{n+1}(\epsilon_{\text{act}}^n), \Pi_h^{n+1}(\epsilon_{\text{inh}}^n)\right) + \widetilde{\boldsymbol{\sigma}}^{n+1}\right) = F^n(\delta \boldsymbol{v}_h) \quad \forall \delta \boldsymbol{v}_h \in \hat{V}_h^{n+1}. \tag{18}$$

In order to correct this issue, a *force coarsening correction term* is computed which compensates for coarsening information loss. The correction term is defined as:

$$C^{n+1}(\delta \boldsymbol{v}_h, \boldsymbol{u}_h^n, \epsilon_{\text{act}}^n, \epsilon_{\text{inh}}^n) := B^n\left(\delta \boldsymbol{v}_h, \Pi_h^{n+1}(\boldsymbol{\sigma}^n)\right) - F^n(\delta \boldsymbol{v}_h) \quad \delta \boldsymbol{v}_h \in \hat{V}_h^{n+1}. \tag{19}$$

This term corresponds to the forces residual obtained by projecting the solution obtained at time n onto the new mesh at time $n+1$, including the stresses correction term $\widetilde{\boldsymbol{\sigma}}^{n+1}$, in the equilibrium equation. When adding (19) to Eq. (18), the resulting weak form is:

$$\begin{aligned} &B^n\left(\delta \boldsymbol{v}_h, \boldsymbol{\sigma}\left(\hat{\boldsymbol{u}}_h^n, \Pi_h^{n+1}(\epsilon_{\text{act}}^n), \Pi_h^{n+1}(\epsilon_{\text{inh}}^n)\right) + \widetilde{\boldsymbol{\sigma}}^{n+1}\right) \\ &= F^n(\delta \boldsymbol{v}_h) + C^{n+1}(\delta \boldsymbol{v}_h, \boldsymbol{u}_h^n, \epsilon_{\text{act}}^n, \epsilon_{\text{inh}}^n) \quad \forall \delta \boldsymbol{v}_h \in \hat{V}_h^{n+1}. \end{aligned} \tag{20}$$

The solution to (20) is $\hat{\boldsymbol{u}}_h^n = P_h^{n+1}(\boldsymbol{u}_h^n)$. By inserting (19) in the formulation, we successfully compensate for information loss in the coarsening process in the equilibrium equation. Note that this means that the solution at time step $n+1$ can be interpreted as the decomposition into:

$$\boldsymbol{u}_h^{n+1} = P_h^{n+1}(\boldsymbol{u}_h^n) + \Delta \boldsymbol{u}_h^{n+1},$$

where the first term is the contribution of the previous time steps with minimum information loss thanks to the modification of the equilibrium equation, and the second one is the increment in displacements caused by the load increments $\Delta \boldsymbol{\epsilon}_{\text{act}}^{n+1}$, $\Delta \boldsymbol{\epsilon}_{\text{inh}}^{n+1}$ at the current step.

By taking into account (19), the resulting finite element problem at time step $n+1$ is: find a displacement field $\boldsymbol{u}_n^{n+1}$ such that:

$$\begin{aligned} &B^{n+1}(\delta \boldsymbol{v}_h, \boldsymbol{\sigma}(\boldsymbol{u}_h^{n+1}, \epsilon_{\text{act}}^{n+1}, \epsilon_{\text{inh}}^{n+1}) + \widetilde{\boldsymbol{\sigma}}^{n+1}) \\ &= F^{n+1}(\delta \boldsymbol{v}_h) + C^{n+1}(\delta \boldsymbol{v}_h, \boldsymbol{u}_h^n, \epsilon_{\text{act}}^n, \boldsymbol{\epsilon}_{\text{inh}}^n) \quad \forall \delta \boldsymbol{v}_h \in V_h^{n+1}. \end{aligned} \tag{21}$$

3.5. Interpretation as a variational multiscale method

The corrections proposed in Subsections 3.3 and 3.4 can be interpreted as a Variational Multiscale approach (see [23]), in which the value of the displacement and stress subscales is exactly known. Let us decompose the solution at time n into its projection onto V_h^{n+1} and the remaining part referred to as the subscales, $\widetilde{\boldsymbol{u}}^n$. This latter corresponds to the information loss in the projection from V_h^n to V_h^{n+1}. Thus:

$$\boldsymbol{u}_h^n = P_h^{n+1}(\boldsymbol{u}_h^n) + \widetilde{\boldsymbol{u}}^n. \tag{22}$$

Similarly, activation and inherent strains are decomposed into:

$$\begin{aligned} \epsilon_{\text{act}}^n &= \Pi_h^{n+1}(\epsilon_{\text{act}}^n) + \widetilde{\epsilon}_{\text{act}}^n, \\ \epsilon_{\text{inh}}^n &= \Pi_h^{n+1}(\epsilon_{\text{inh}}^n) + \widetilde{\epsilon}_{\text{inh}}^n. \end{aligned} \tag{23}$$

Eq. (16) straightforwardly defines the stress subscales $\widetilde{\boldsymbol{\sigma}}$.

Correction stresses $\widetilde{\boldsymbol{\sigma}}$ and correction forces $C^{n+1}(\delta \boldsymbol{v}_h, \boldsymbol{u}_h^n, \epsilon_{\text{act}}^n, \epsilon_{\text{inh}}^n)$ precisely account for the (otherwise lost) contribution of $\widetilde{\boldsymbol{u}}^n$, $\widetilde{\boldsymbol{\epsilon}}_{\text{act}}^n$, $\widetilde{\epsilon}_{\text{inh}}^n$, and $\widetilde{\boldsymbol{\sigma}}$ to the bilinear form. This interpretation gives a variational foundation to the proposed correction terms.

4. Numerical examples

In this section some numerical examples illustrate the performance of the proposed methodology.

The objectives are two-fold: (a) to reduce the computational effort using mesh refinement and, particularly, mesh coarsening, and (b) to minimize the effects induced by the mesh coarsening using the proposed correction terms. Both the CPU-time and the result accuracy using the mesh adaptivity *with* and *without* the correction term are compared to a fixed fine FE mesh used as a reference. These numerical examples do not pretend to present accurate results for the quantities of interest of a particular simulation (the used finite element meshes are possibly too coarse for this), but on the contrary they have been selected because they are illustrative and allow us to show the improvements that can be obtained by using the strategy proposed in this work.

The material and process parameters used in the numerical examples are shown in Table 1 and the building process follows a layer-by-layer activation scheme.

Three test-cases are proposed. The first one adopts a fixed computational domain and it is intended to demonstrate the necessity of the correction term to preserve the solution obtained with the finest mesh used in the adaptive process. The second example shows the virtue of the adaptive technology when a growing computational domain is used as required for the simulation of the AM process. Finally, an industrial component is simulated with the proposed technology to show the speed-up obtained with respect to the use of a fixed mesh while preserving the same accuracy.

To assess the global error of each example, a *relative* L^2 *error* norm of the displacement field is computed at the end of the simulation as:

$$e_{L^2} = \frac{\sqrt{\int_\Omega \left(P_h^{\text{coarse}}(\boldsymbol{u}_h^{\text{fine}}) - \boldsymbol{u}_h^{\text{coarse}}\right) d\Omega}}{\sqrt{\int_\Omega \left(P_h^{\text{coarse}}(\boldsymbol{u}_h^{\text{fine}})\right)^2 d\Omega}} \tag{24}$$

where $P_h^{\text{coarse}}(\boldsymbol{u}_h^{\text{fine}})$ is the projection of the reference (fixed fine mesh) solution and $\boldsymbol{u}_h^{\text{coarse}}$ is the solution obtained with the coarsened mesh both *with* and *without* the correction term.

Remark: Note that the error is computed after point to point projecting the fine solution onto the coarse mesh: this is so because the objective of the methodology is to avoid any spurious displacement due to the coarsening of lower layers to be transferred to the upper layers, where the printing is taking place and which have still not been coarsened. This translates into trying to minimize the difference between the fine and the coarse solutions on the degrees of freedom which have not

Table 1
Simulation parameters.

Parameter	Cantilever Beam	Slender Column	Gear Component
Young's Modulus (E)	100 GPa	100 GPa	100 GPa
Poisson's ratio (ν)	0.3	0.3	0.3
Density (ρ)	4420 kg/m^3	4420 kg/m^3	4420 kg/m^3
Layer thickness (t)	(−)	0.10 mm	1 mm
Refinement height (h_{ref})	3 m	0.5 mm	1 mm
$\epsilon_{inh}^x = \epsilon_{inh}^y$	(−)	-0.67	-0.67
ϵ_{inh}^z	(−)	0.0	0.0

been coarsened, and hence the proposed definition of the relative *L2 error* norm.

The numerical simulations are carried out using the FEMUSS (*Finite Element Method Using Subgrid Scales*) software developed by the authors at the International Center for Numerical Methods in Engineering (CIMNE). The post-processing is done using Paraview [1].

4.1. Cantilever beam

This example demonstrates the necessity of using the proposed correction terms to retain the solution accuracy of the finest mesh used when a coarsening strategy is employed, in a very simple setting. The objective is to observe how, for a single simulation step, information is transferred from a fine to a coarse mesh thanks to the correction terms. As it will be shown, if no coarsening correction terms are used all the information on the solution obtained in the fine mesh is lost when coarsening. On the contrary, if the correction terms are used, optimal projected solutions for both displacements and stresses on the coarse mesh are obtained.

The dimensions of a slender cantilever beam are reported in Fig. 4. The beam is clamped at one end and subjected to its self-weight, only. The reference solution is obtained using a uniform mesh with an element size: $h = 6.25$ mm. The adaptive strategy starts from the same fine mesh. Once the solution is obtained, a coarsening step increases the element size up to 50 mm (see Fig. 5). Next, the simulation is repeated on the new coarse mesh. This is done both for a trilinear hexahedra mesh and for a linear tetrahedra mesh.

Figs. 6 and 7 compare the magnitudes of the vertical displacements for the fine mesh, coarse mesh *without* and coarse mesh *with* the correction terms for the hexahedra and tetrahedra cases respectively. Figs. 8 and 9 do the same comparison for the normal stresses in the main bending direction.

In both the hexa and tetrahedra cases the solution in the coarse mesh achieved *without* the correction terms is too stiff because of the very poor finite element approximation space. This are simply new simulations on the coarse meshes, and they do not take advantage of the information obtained in the first step of the simulation on the fine mesh. Also, the obtained stress fields are poor, this can be clearly observed in the tetrahedra mesh stress plot, where the stress field is constant element to element and presents large jumps between adjacent elements. On the hexahedra elements, the stresses are also discontinuous element to element, but they have a linear component in space, so the effect is not so apparent.

On the contrary, when the correction terms are used, the information on the fine mesh is transferred to the coarser mesh, and the agreement with the reference solution is optimal (for this single step simulation displacements (in the nodes) and stresses (at the integration points) are identical in the fine and the coarse meshes except for projection errors). In the stress field plot, it is worth observing that for linear tetrahedra, stresses are no longer constant element to element thanks to the correction terms.

The global errors are presented in Table 2 where the corresponding *relative* L^2 *error* norms are computed according to equation 24. As expected, the error is null for the coarse mesh if the coarsening correction terms are employed.

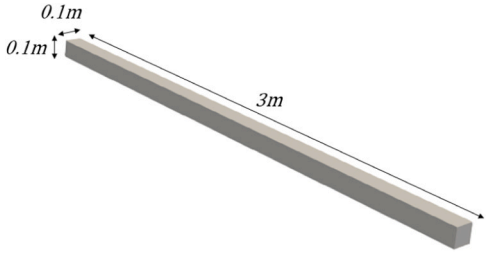

Fig. 4. Cantilever beam: Geometry and dimensions.

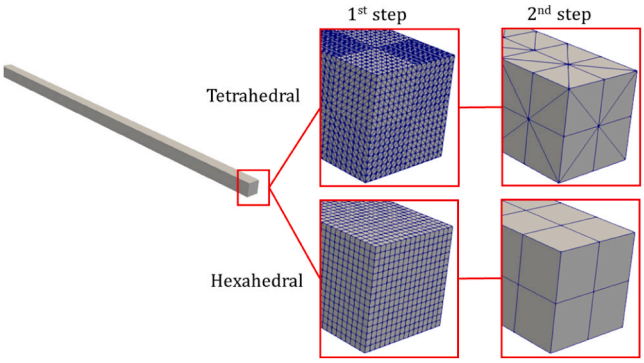

Fig. 5. Cantilever beam: fine (reference) and coarse meshes.

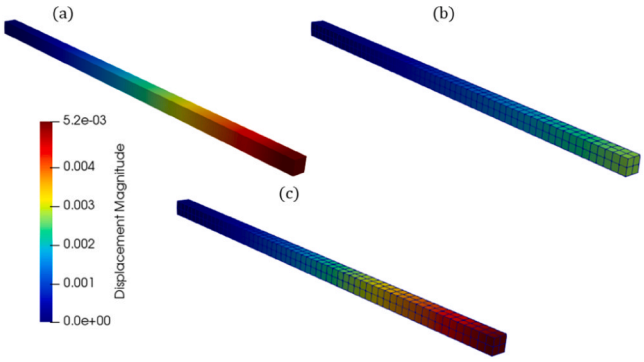

Fig. 6. Cantilever beam: Displacement results for the hexahedral mesh. (a) Fine mesh. (b) Adaptive mesh *without* correction terms. (c) Adaptive mesh *with* correction terms.

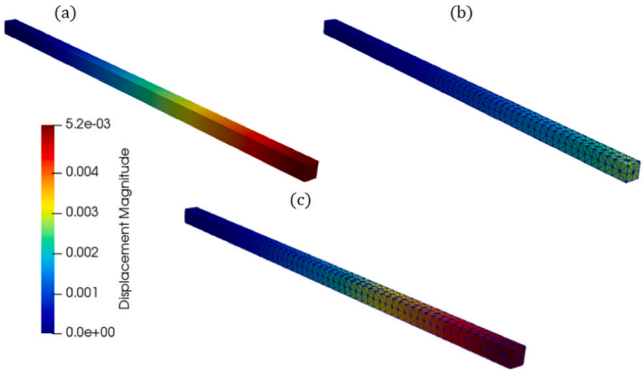

Fig. 7. Cantilever beam: Displacement results for the tetrahedral mesh. (a) Fine mesh. (b) Adaptive mesh *without* correction terms. (c) Adaptive mesh *with* correction terms.

The key point of the methodology is that if a new load increment was now solved on the coarse mesh, the resulting displacement and stress increments would be computed on such current coarse mesh. However, the displacement and stress increments associated to the original load, which were computed on the fine mesh, would not loose the fine mesh accuracy. This is especially important in AM simulations where elements will be concentrated dynamically in the region of the melting-pool (TMAZ).

4.2. Slender column

This example proves the efficiency of the coarsening strategy to

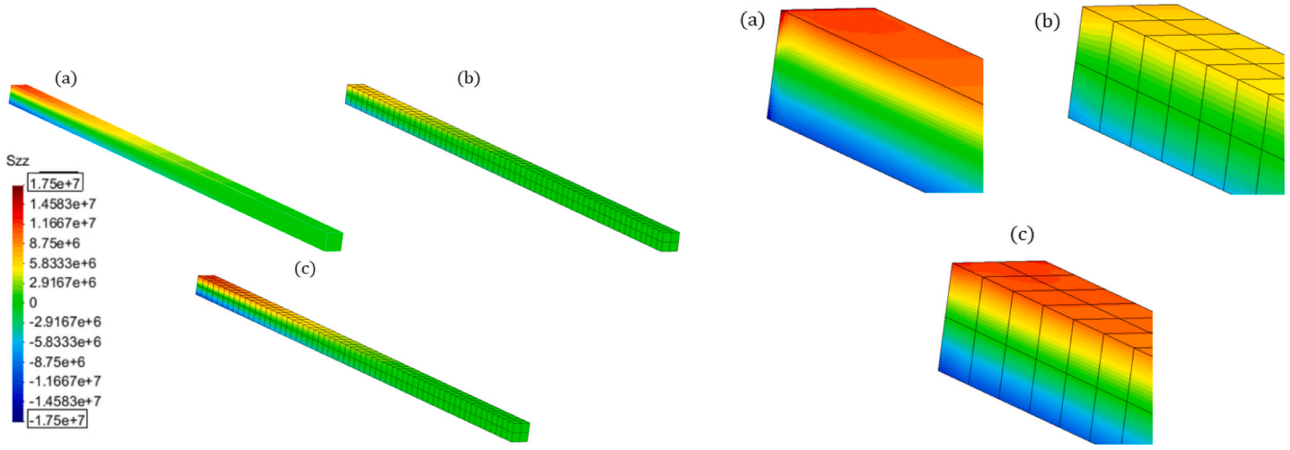

Fig. 8. Cantilever beam: Stress results for the hexahedra mesh. (a) Fine mesh. (b) Adaptive mesh *without* correction terms. (c) Adaptive mesh *with* correction terms.

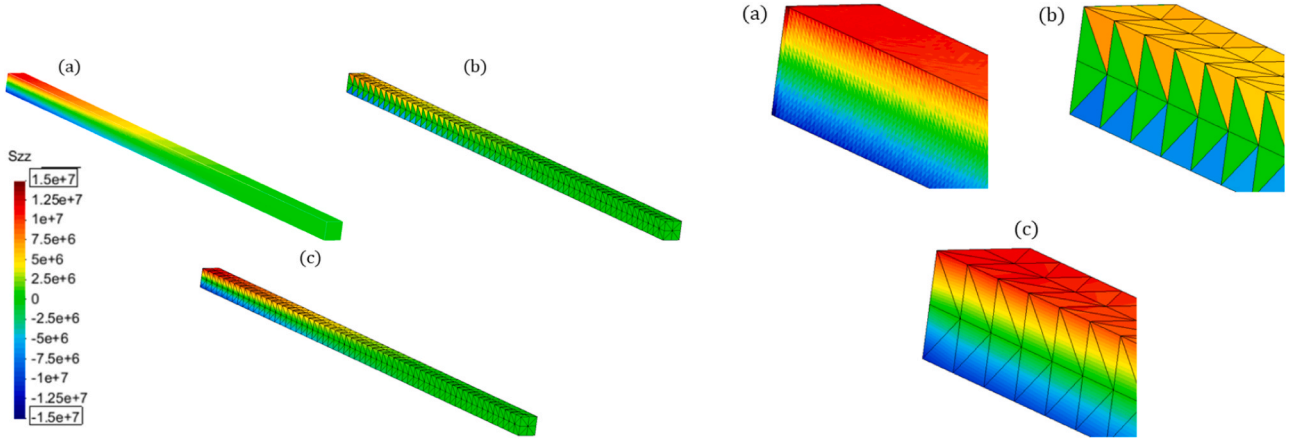

Fig. 9. Cantilever beam: Stress results for the tetrahedra mesh. (a) Fine mesh. (b) Adaptive mesh *without* correction terms. (c) Adaptive mesh *with* correction terms.

Table 2
Cantilever beam: relative global error e_{L^2} norm.

Model	Hexahedra	Tetrahedra
Adaptive mesh *without* correction term	46.9%	50.0%
Adaptive mesh *with* correction term	0%	0%

analyse growing domains as required for the numerical simulation of the AM process. This is particularly necessary when using the layer-by layer activation technique and slender parts.

The selected geometry consists of a 10 mm high column of 1×1 mm^2 square base. A total number of 100 layers are activated in 100 time-steps. Two different solutions are compared in Fig. 10: (a) a uniform mesh characterized by an element size: $h = 0.03125$ mm and, (b) an adaptive mesh having the same element size within the process region and a maximum coarsening up to $h = 0.5$ mm. The finer discretization follows the activation process to maintain the highest resolution in the TMAZ while a coarser mesh is adopted elsewhere.

Fig. 11 shows the evolution of the displacements *with* and *without* the proposed correction term at point P situated at coordinates (0, 0, 1) mm (see Fig. 10). The adaptive solutions are compared to the solution obtained with the fine fixed mesh used as a reference. It is observed that *without* the correction term the cumulative error is between 20% (x and y components) and 40% (z component), while the difference is between 2% (x and y components) and 8% (z component) when using the correction strategy.

Fig. 12 shows the plot of the displacement and stress fields at the end

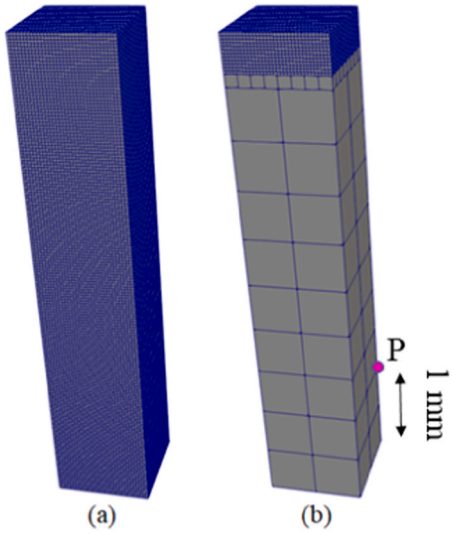

Fig. 10. Slender column: (a) Fixed mesh with hexahedral elements. (b) Adaptive meshing at the end of the simulation and position of point P.

of the simulation for the fixed and adaptive meshes. Regarding displacements, it can be observed that the adaptive solution *with* correction terms ensures that the nodal values are much closer to the solution of the fine mesh during the whole simulation. The improvement is even more

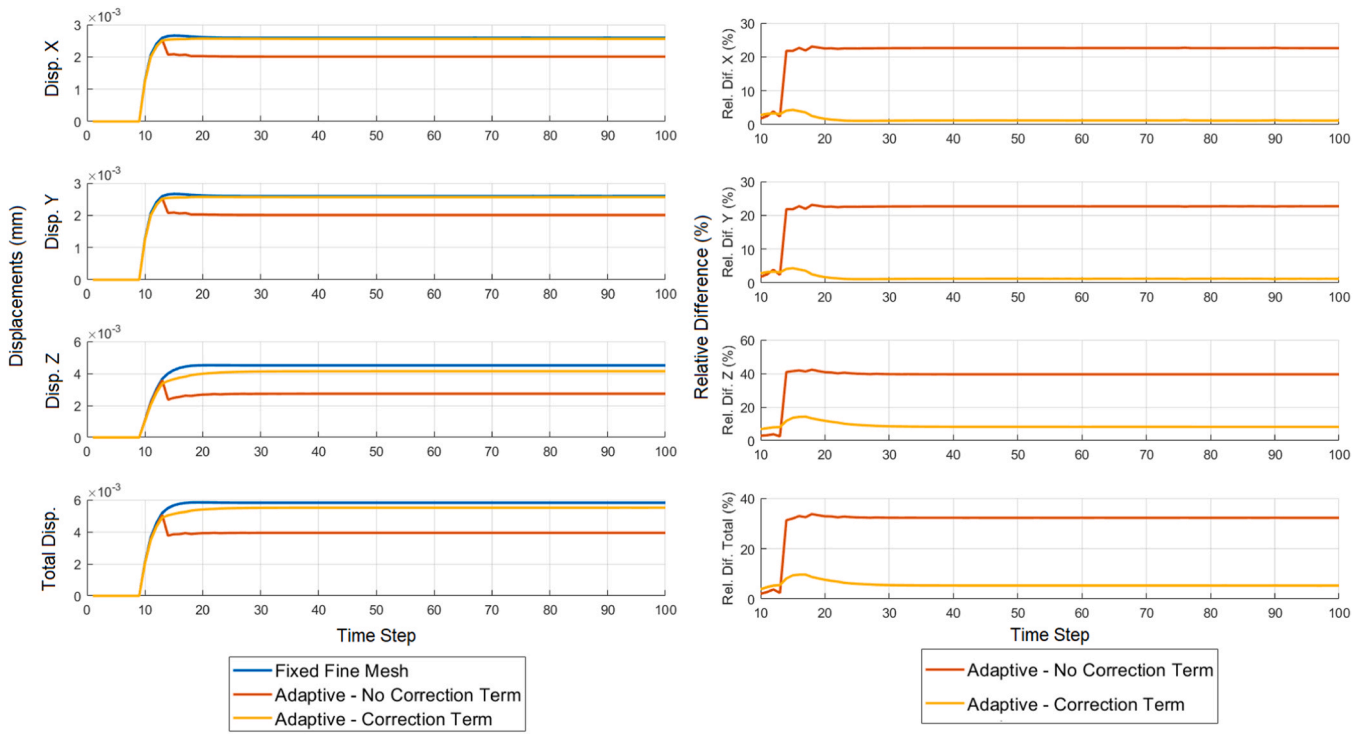

Fig. 11. Slender column: Evolution of the displacements (*left*) and the relative difference vs. the fixed fine mesh (*right*) at point *P* during the activation process.

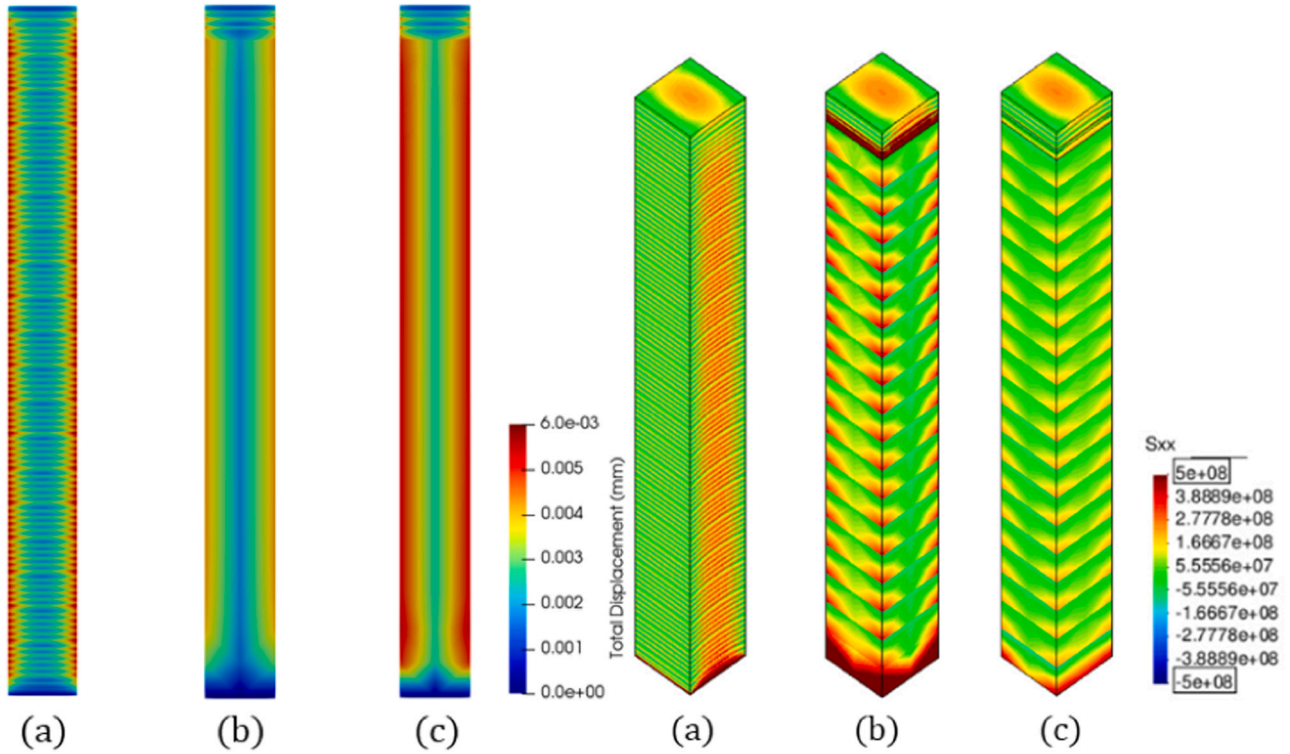

Fig. 12. Slender column: Displacement (left) and stress (right) fields at the end of the simulation. (a) Fine mesh. (b) Adaptive mesh *without* correction terms. (c) Adaptive mesh *with* correction terms.

relevant in the stresses case. A remarkable generalized lack of global accuracy in the stress computation is observed in the adaptive case *without* correction term, with a spurious stress jump in the interface between the fine and coarse mesh areas in the top of the column. This spurious stress jump is caused by the switching of free nodes to hanging nodes in the coarsening process as explained in Section 3.3. The adaptive simulation *with* correction terms, on the contrary, shows a very good agreement with the fine mesh simulation (except for the expected and unavoidable loss of resolution due to extreme coarsening). Fig. 13 compares the CPU-time and the number of active nodes (mesh size)

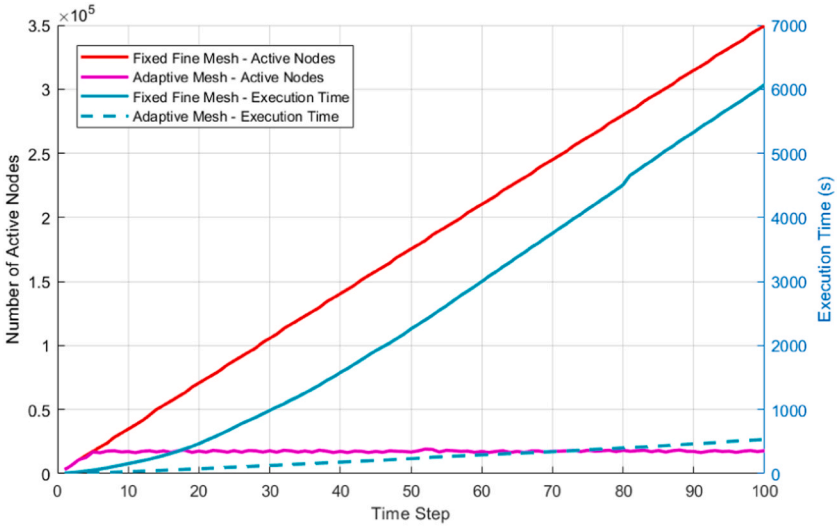

Fig. 13. Slender column: Number of active nodes (*left y-axis*) and execution time (*right y-axis*) comparison between fixed and adaptive meshes.

using the fixed and the adaptive meshes. During the activation of the first 5 layers, the two strategies adopt the same mesh and consequently approximately the same solution time is required. Next, the adaptive strategy is switched on. Thereafter, the mesh size (number of active nodes) of the adaptive mesh is kept almost constant allowing for a reduced CPU-time increment for each new time-step. Contrarily, the fixed mesh requires an increasing amount of resources as the growing process proceeds. Therefore, the use of a fixed mesh is not recommended for the numerical simulation of industrial AM processes and, particularly, when the high-fidelity simulation of the actual layer thickness and the detailed scanning sequence is required.

4.3. Gear component

The last example corresponds to an industrial component: a gear 17 mm high with an outer diameter of 40 mm. The gear is attached to the base-plate, thus the movements of all the nodes belonging to its lower surface are prescribed. The computational domain is discretized by an unstructured tetrahedral mesh. On the one hand, a fixed coarse mesh is generated with an average element size of 0.70 mm and a total number of 880, 384 elements and 169, 316 nodes. On the other hand, a fine mesh (used as the numerical reference) is characterized by an average mesh size of 0.35 mm and a total number of elements 7, 470, 787 and 1, 259, 626 nodes. Finally, the adaptive mesh adopts the same mesh size as the fine mesh within the process zone (defined as the volume enclosed up to a vertical distance h_{ref}) and it is coarsened up to the size of the fixed coarse mesh elsewhere (see Fig. 15). In this case, the average mesh includes about 493, 058 nodes and 2, 743, 781 elements.

The *P* point on the external surface, at 4.3 mm from the base plate, is chosen to record the evolution of the radial displacement on the different meshes used (see Fig. 14). The layer thickness is 1 mm so that 17 time-steps are required to complete the AM process. Note that the layer thickness chosen is the minimal to allow for the use of the fixed fine mesh (adopted as the numerical reference) in a reasonable CPU-time. Fig. 16 shows the total displacement magnitude at the end of the simulation for the four adopted meshes. Fig. 17 shows the difference

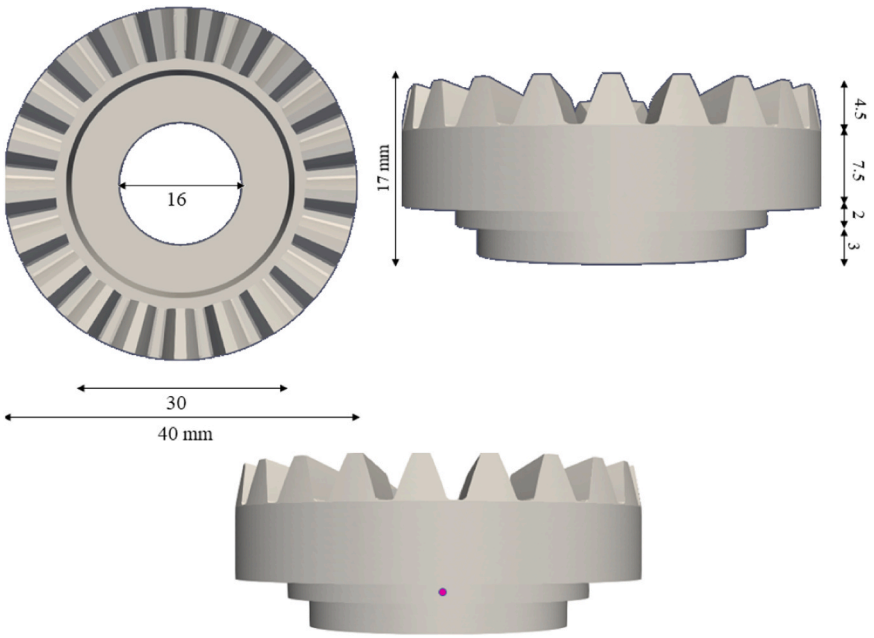

Fig. 14. Gear component: Geometry and position of the reference point *P*.

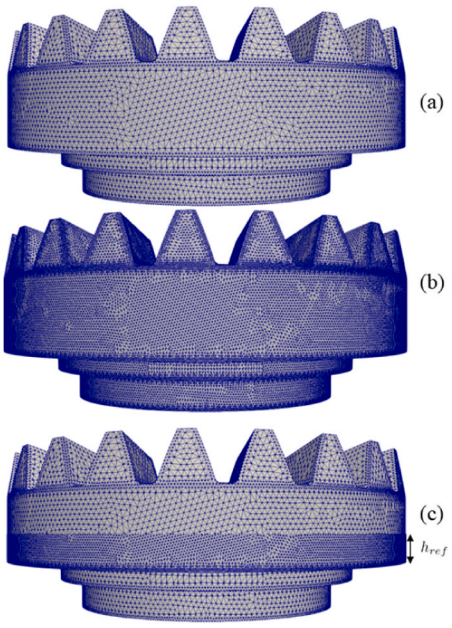

Fig. 15. Gear component: (a) Fixed coarse mesh. (b) Fixed fine mesh. (c) Adaptive mesh.

between such displacement and the displacement on the reference fine mesh. As expected accuracy is better for the adaptive simulation *with* correction terms. Fig. 18(*a*) shows the evolution of the radial displacements at point P using both the fixed fine and coarse meshes and the adaptive solution *with* and *without* the correction term. Fig. 18(*b*) presents the corresponding relative error with respect to the fixed fine mesh. Once again, the agreement of the adaptive solution with the proposed correction with the fine mesh is remarkable. The relative local error is lower than 2.50% while a standard adaptivity without the correction shows a local error of about 14%.

The global error analysis is presented in Fig. 17: the errors are computed as the difference between the reference solution (fixed fine mesh) and the results obtained with the coarse mesh and the adaptive technology, and projected on the coarse mesh for their visualization. Table 3 provides the global *r*elative L^2 error computed according to equation 24: the corrected methodology increases the global accuracy of about 40% with respect to the crude adaptivity and of about 70% with respect to the solution obtained with the fixed coarse mesh.

Fig. 19 shows the Von-Mises stress field at a cut along the central plane of the gear component. The results from the fixed coarse and fine meshes are quite similar. However, the adaptive mesh *without* the correction terms approximates the Von-Mises stress field very poorly. The reason for this is that linear tetrahedral elements are used in this simulation. Due to this, the activation strain field, computed from the gradient of an initial displacement field as defined in Section 2, presents heavy jumps from element to element in the adaptive mesh prior to coarsening. This is illustrated in Fig. 20. When coarsened, the projected activation strain field on the coarse mesh is assigned an averaged value

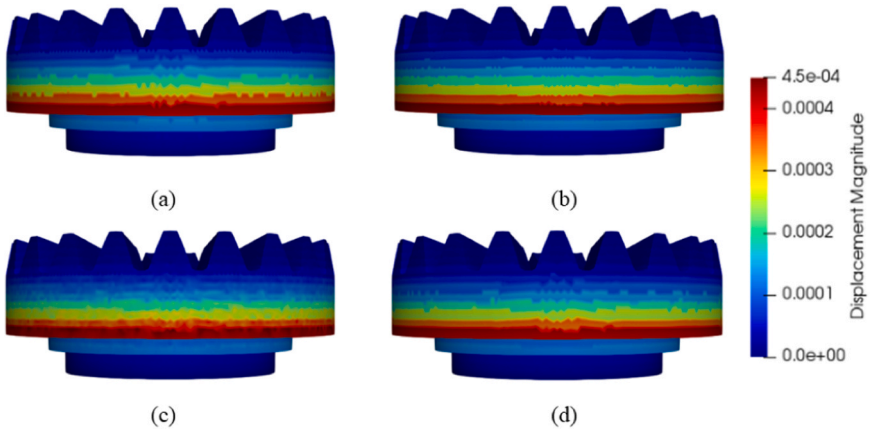

Fig. 16. Gear: Final displacement. (a) Fixed coarse mesh. (b) Fixed Fine mesh. (c) Adaptive mesh *without* correction terms. (d) Adaptive mesh *with* correction terms.

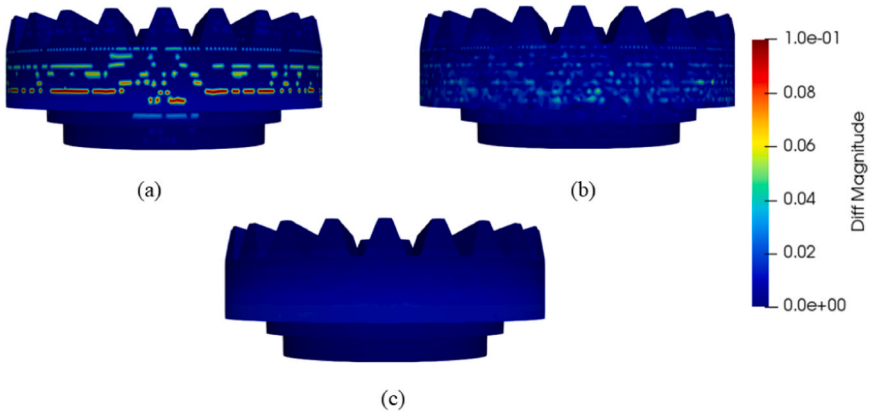

Fig. 17. Gear: Displacement relative difference w.r.t reference mesh projected onto the coarse mesh. (a) Fixed coarse mesh. (b) Adaptive mesh *without* correction terms. (c) Adaptive mesh *with* correction terms.

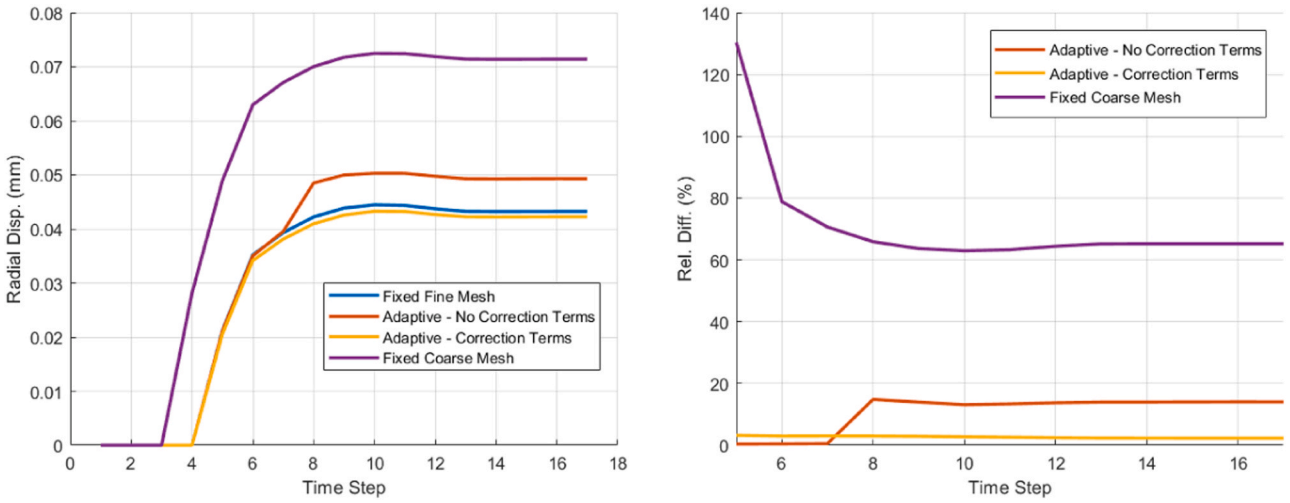

Fig. 18. Gear: evolution of the radial displacement at point P (*left*) and the relative difference with respect to the fixed fine mesh (*right*).

Table 3
Gear: relative global error e_{L^2} norm.

Model	Relative e_{L^2} norm
Fixed coarse mesh	11.9%
Adaptive mesh *without* correction term	5.9%
Adaptive mesh *with* correction term	3.6%

(Fig. 20 (b), (c)). This averaged value is used together with the displacement field in order to compute stresses, and this results in a very poor approximation, as shown in Fig. 19 (c). By using the stress correction terms this phenomenon is corrected, resulting in the stress field presented in Fig. 19 (d), which is pretty much the projection of the fine mesh stress field in Fig. 19 (b) onto the coarsened adaptive mesh.

Fig. 21 shows graphically the computational efficiency of the proposed adaptive technology in terms of CPU-time and maximum memory consumed during the simulation. In terms of solution time a speed-up of 2.25 with respect to the fixed fine solution is obtained. This speed-up can be increased by reducing the size of the moving fine mesh which is following the TMAZ. In the actual process the heat penetration is of about 2–3 layer thickness. Therefore, the mesh refinement can be reduced to this size, only. Finally, observe that the computational cost due to the evaluation of the correction term is negligible allowing for its use for any mesh discretization.

5. Conclusions

In this work an adaptive FE strategy to deal with the numerical simulation of AM processes has been presented. An octree-based mesh adaptivity approach has been adopted allowing for the use of much finer meshes within the processing zone, the TMAZ, if compared to the rest of the computational domain. Although the adaptive meshing is vital to keep the computational resources bounded through the entire simulation of the fabrication process, the accuracy of the results can be compromised by the coarsening strategy. This loss of accuracy can spoil the original efforts in refining the mesh in the process zone. Therefore a strategy to compensate for information loss in the adaptive refinement

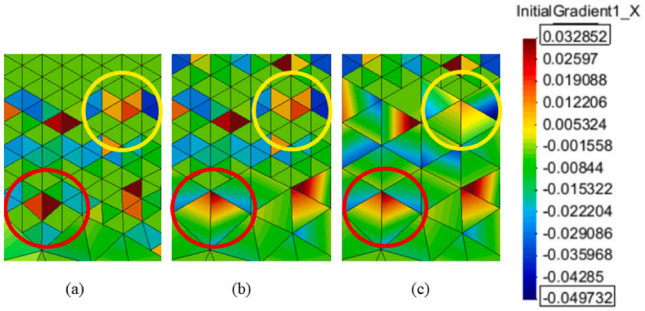

Fig. 20. Evolution of $\boldsymbol{\epsilon}_{\text{inh}} + \boldsymbol{\epsilon}_{\text{act}}$ fields, ϵ^x component, on a tetrahedral mesh through the coarsening process.

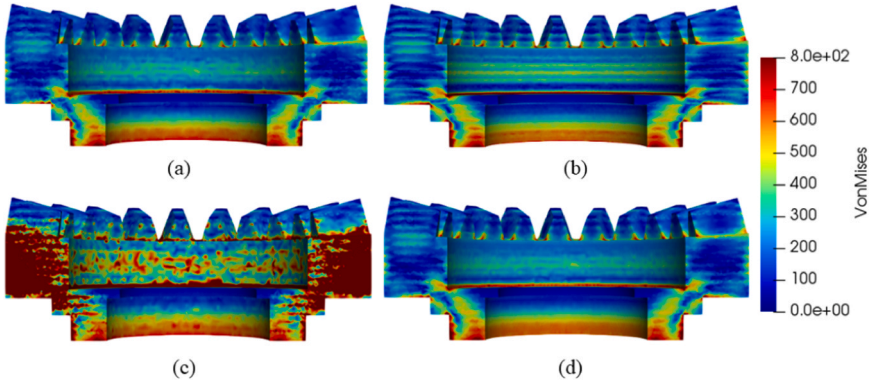

Fig. 19. Gear: Von-Misses stress at a cut along the central plane. (a) Fixed coarse mesh. (b) Fixed Fine mesh. (c) Adaptive mesh *without* correction terms. (c) Adaptive mesh *with* correction terms.

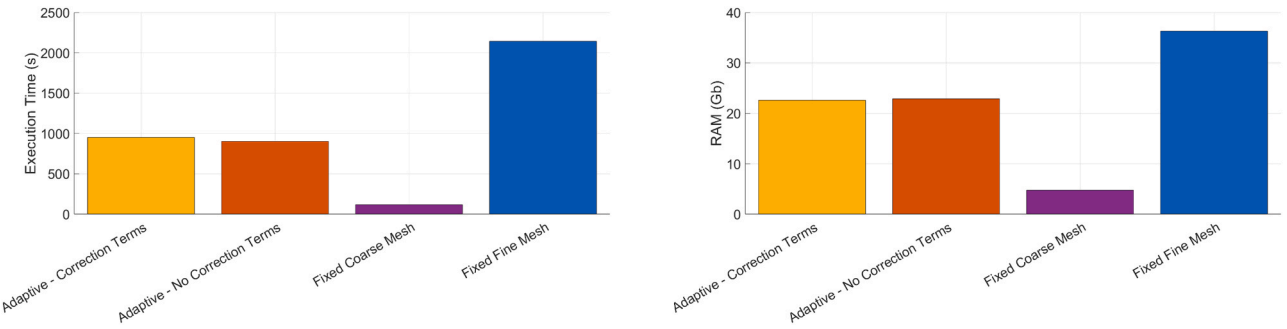

Fig. 21. Gear: Comparison of CPU-time (*left*) and maximum memory consumption (*right*) between adopted models.

simulation of additive manufacturing processes is developed.

The main idea is to add two correction terms which compensate for the loss of accuracy in the coarsening process of the mesh in already manufactured regions. The first term corrects the errors introduced in the stress field by the coarsening process. The second correction term consists of a forcing term introduced in the weak form of the problem which prevents loss of information in the displacement field. This allows to successfully simulate the additive manufacturing process by using an adaptively coarsened mesh, with results which have an accuracy very similar to the one of a uniformly refined mesh simulation, at a fraction of the computational cost. Also, the proposed correction terms can be interpreted as a Variational Multiscale enhancement on the adaptive mesh, which gives a variational foundation to the proposed correction strategy.

The numerical examples show the generality of the proposed methodology, which has been applied to different FE meshes, AM processes, several geometries, and its success in reducing the overall computational cost. The coarsening correction terms have turned out to be key in order to obtain a good accuracy in the simulation.

The ideas presented in this work can be extended to more complex problems such as coupled thermo-mechanical simulations including non-linear behavior like plastic or damage constitutive models. This will be a matter of future work.

Declaration of Competing Interest

The authors declare that they have no known financial interests or personal relationships that could have appeared to influence the work reported in this paper.

Acknowledgments

J. Baiges gratefully acknowledges the support of the Spanish Government through the Ramón y Cajal grant RYC-2015-17367. R. Codina gratefully acknowledges the support received through the ICREA Acadèmia Research Program of the Catalan Government. The financial support from the Spanish Ministry of Economy and Competitiveness, through the Severo Ochoa Programme for Centres of Excellence in R&D (CEX2018-000797-S), is gratefully acknowledged. The authors also acknowledge the financial support provided by the Spanish Ministry of Economy via the ADaMANT project (DPI2017-85998-P): Computational Framework for Additive Manufacturing of Titanium Alloy.

References

[1] J. Ahrens, B. Geveci, C. Law, ParaView: An End-User Tool for Large Data Visualization. Visualization Handbook, Elsevier, 2005.
[2] F. Armero, J.C. Simo, A new unconditionally stable fractional step method for non-linear coupled thermomechanical problems, Int. J. Numer. Methods Eng. 35 (4) (1992) 737–766.
[3] J. Baiges, C. Bayona, Refficientlib: an efficient load-rebalanced adaptive mesh refinement algorithm for high-performance computational physics meshes, SIAM J. Sci. Comput. 39 (2) (2017) 65–95.
[4] J. Baiges, R. Codina, Variational multiscale error estimators for solid mechanics adaptive simulations: an orthogonal subgrid scale approach, Comput. Methods Appl. Mech. Eng. 325 (2017) 37–55.
[5] J. Baiges, R. Codina, I. Castañar, E. Castillo, A finite element reduced-order model based on adaptive mesh refinement and artificial neural networks, Int. J. Numer. Methods Eng. 121 (4) (2020) 588–601.
[6] J. Baiges, R. Codina, S. Idelsohn, Reduced-order subscales for POD models, Comput. Methods Appl. Mech. Eng. 291 (2015) 173–196.
[7] J. Baiges, J. Martínez-Frutos, D. Herrero-Pérez, F. Otero, A. Ferrer, Large-scale stochastic topology optimization using adaptive mesh refinement and coarsening through a two-level parallelization scheme, Comput. Methods Appl. Mech. Eng. 343 (2019) 186–206.
[8] J.L. Bartlett, X. Li, An overview of residual stresses in metal powder bed fusion, Addit. Manuf. 27 (2019) 131–149.
[9] M. Bugatti, Q. Semeraro, Limitations of the inherent strain method in simulating powder bed fusion processes, Addit. Manuf. 23 (2018) 329–346.
[10] M. Cervera, C. Agelet De Saracibar, M. Chiumenti, Thermo-mechanical analysis of industrial solidification processes, Int. J. Numer. Methods Eng. 46 (9) (1999) 1575–1591.
[11] Q. Chen, X. Liang, D. Hayduke, J. Liu, L. Cheng, J. Oskin, R. Whitmore, A. To, inherent strain based multiscale modeling framework for simulating part-scale residual deformation for direct metal laser sintering, Addit. Manuf. 28 (2019) 406–418.
[12] B. Cheng, S. Shrestha, K. Chou, Stress and deformation evaluations of scanning strategy effect in selective laser melting, Addit. Manuf. 12 (2016) 240–251.
[13] M. Chiumenti, C. Agelet de Saracibar, M. Cervera, On the numerical modeling of the thermomechanical contact for metal casting analysis, J. Heat Transf. 130 (6) (2008), 061301.
[14] M. Chiumenti, M. Cervera, N. Dialami, B. Wu, L. Jinwei, C. Agelet de Saracibar, Numerical modeling of the electron beam welding and its experimental validation, Finite Elem. Anal. Des. 121 (2016) 118–133.
[15] M. Chiumenti, M. Cervera, A. Salmi, C.D. Saracibar, N. Dialami, K. Matsui, Finite element modeling of multi-pass welding and shaped metal deposition processes, Comput. Methods Appl. Mech. Eng. 199 (37–40) (2010) 2343–2359.
[16] M. Chiumenti, X. Lin, M. Cervera, W. Lei, Y. Zheng, W. Huang, Numerical simulation and experimental calibration of additive manufacturing by blown powder technology. Part I: thermal analysis, Rapid Prototyp. J. 23 (2) (2017) 448–463.
[17] M. Chiumenti, E. Neiva, E. Salsi, M. Cervera, S. Badia, J. Moya, Z. Chen, C. Lee, C. Davies, Numerical modelling and experimental validation in selective laser melting, Addit. Manuf. 18 (2017) 171–185.
[18] E.R. Denlinger, M. Gouge, J. Irwin, P. Michaleris, Thermomechanical model development and in situ experimental validation of the laser powder-bed fusion process, Addit. Manuf. 16 (2017) 73–80.
[19] E.R. Denlinger, J.C. Heigel, P. Michaleris, Residual stress and distortion modeling of electron beam direct manufacturing Ti-6Al-4V, Proc. Inst. Mech. Eng. Part B J. Eng. Manuf. 229 (10) (2015) 1803–1813.
[20] E.R. Denlinger, J. Irwin, P. Michaleris, Thermomechanical modeling of additive manufacturing large parts, J. Manuf. Sci. Eng. 136 (6) (2014).
[21] M. Gouge, E. Denlinger, J. Irwin, C. Li, P. Michaleris, Experimental validation of thermo-mechanical part-scale modeling for laser powder bed fusion processes, Addit. Manuf. 29 (2019), 100771.
[22] M. Hill, D. Nelson, The inherent strain method for residual stress determination and its application to a long welded joint, ASME-Publ.-PVP 318 (1995) 343–352.
[23] T. Hughes, G. Feijóo, L. Mazzei, J. Quincy, The variational multiscale method-a paradigm for computational mechanics, Comput. Methods Appl. Mech. Eng. 166 (1–2) (1998) 3–24.
[24] T.-S. Jun, A.M. Korsunsky, Evaluation of residual stresses and strains using the eigenstrain reconstruction method, Int. J. Solids Struct. 47 (13) (2010) 1678–1686.
[25] K. Khan, A. De, Modelling of selective laser melting process with adaptive remeshing, Sci. Technol. Weld. Join. 24 (5) (2019) 391–400.
[26] S. Kollmannsberger, A. Özcan, M. Carraturo, N. Zander, E. Rank, A hierarchical computational model for moving thermal loads and phase changes with applications to selective laser melting, Comput. Math. Appl. 75 (5) (2018) 1483–1497.

[27] C. Li, E.R. Denlinger, M.F. Gouge, J.E. Irwin, P. Michaleris, Numerical verification of an octree mesh coarsening strategy for simulating additive manufacturing processes, Addit. Manuf. 30 (2019), 100903.
[28] X. Liang, Q. Chen, L. Cheng, D. Hayduke, A.C. To, Modified inherent strain method for efficient prediction of residual deformation in direct metal laser sintered components, Comput. Mech. 64 (6) (2019) 1719–1733.
[29] X. Liang, L. Cheng, Q. Chen, Q. Yang, A.C. To, A modified method for estimating inherent strains from detailed process simulation for fast residual distortion prediction of single-walled structures fabricated by directed energy deposition, Addit. Manuf. 23 (2018) 471–486.
[30] X. Liang, W. Dong, S. Hinnebusch, Q. Chen, H.T. Tran, J. Lemon, L. Cheng, Z. Zhou, D. Hayduke, A.C. To, Inherent strain homogenization for fast residual deformation simulation of thin-walled lattice support structures built by laser powder bed fusion additive manufacturing, Addit. Manuf. 32 (2020), 101091.
[31] L.-E. Lindgren, A. Lundback, M. Fisk, R. Pederson, J. Andersson, Simulation of additive manufacturing using coupled constitutive and microstructure models, Addit. Manuf. 12 (2016) 144–158 (Special Issue on Modeling and Simulation for Additive Manufacturing).
[32] X. Lu, X. Lin, M. Chiumenti, M. Cervera, Y. Hu, X. Ji, L. Ma, W. Huang, In situ measurements and thermo-mechanical simulation of ti-6al-4v laser solid forming processes, Int. J. Mech. Sci. 153–154 (2019) 119–130.
[33] X. Lu, X. Lin, M. Chiumenti, M. Cervera, Y. Hu, X. Ji, L. Ma, H. Yang, W. Huang, Residual stress and distortion of rectangular and s-shaped ti-6al-4v parts by directed energy deposition: modelling and experimental calibration, Addit. Manuf. 26 (2019) 166–179.
[34] X. Lu, X. Lin, M. Chiumenti, M. Cervera, J. Li, L. Ma, L. Wei, Y. Hu, W. Huang, Finite element analysis and experimental validation of the thermomechanical behavior in laser solid forming of ti-6al-4v, Addit. Manuf. 21 (2018) 30–40.
[35] H. Murakawa, Y. Luo, Y. Ueda, Inherent Strain as an Interface Between Computational Welding Mechanics and its Industrial Application, 1998, pp. 597–619. Book Inst. Mater.
[36] E. Neiva, S. Badia, A.F. Martín, M. Chiumenti, A scalable parallel finite element framework for growing geometries. Application to metal additive manufacturing, Int. J. Numer. Methods Eng. 119 (11) (2019) 1098–1125.
[37] E. Neiva, M. Chiumenti, M. Cervera, E. Salsi, G. Piscopo, S. Badia, A.F. Martín, Z. Chen, C. Lee, C. Davies, Numerical modelling of heat transfer and experimental validation in powder-bed fusion with the virtual domain approximation, Finite Elem. Anal. Des. 168 (2020), 103343.
[38] A. Olleak, Z. Xi, Efficient lpbf process simulation using finite element modeling with adaptive remeshing for distortions and residual stresses prediction, Manuf. Lett. 24 (2020) 140–144.
[39] D. Pal, N. Patil, K.H. Kutty, K. Zeng, A. Moreland, A. Hicks, D. Beeler, B. Stucker, A generalized feed-forward dynamic adaptive mesh refinement and derefinement finite-element framework for metal laser sintering-part II: nonlinear thermal simulations and validations2, J. Manuf. Sci. Eng. 138 (6) (2016), 061003.
[40] L. Parry, I. Ashcroft, R. Wildman, Understanding the effect of laser scan strategy on residual stress in selective laser melting through thermo-mechanical simulation, Addit. Manuf. 12 (2016) 1–15.
[41] N. Patil, D. Pal, H. KhalidRafi, K. Zeng, A. Moreland, A. Hicks, D. Beeler, B. Stucker, A generalized feed forward dynamic adaptive mesh refinement and derefinement finite element framework for metal laser sintering-part I: formulation and algorithm development, J. Manuf. Sci. Eng. 137 (4) (2015), 041001.
[42] D. Riedlbauer, P. Steinmann, J. Mergheim, Thermomechanical finite element simulations of selective electron beam melting processes: performance considerations, Comput. Mech. 54 (2014) 109–122.
[43] I. Setien, M. Chiumenti, S. van der Veen, M.S. Sebastian, F. Garciandía, A. Echeverría, Empirical methodology to determine inherent strains in additive manufacturing, Comput. Math. Appl. 78 (2019) 2282–2295.
[44] T. Terasaki, T. Akiyama, Mechanical behaviour of joints in FSW: residual stress, inherent strain and heat input generated by friction stir welding, Weld. World 47 (2003) 24–31.
[45] Y. Ueda, Y. Kim, A. Umekuni, Measuring theory of three-dimensional residual stresses using a thinly sliced plate perpendicular to welded line, Trans. JWRI 14 (2) (1985) 151–157.
[46] Y. Ueda, H. Murakawa, N. Ma, Welding Deformation and Residual Stress Prevention, Elsevier, 2012.
[47] Y. Ueda, H. Murakawa, K. Nakacho, N. Ma, Establishment of computational welding mechanics, Weld. Surf. Rev. 8 (1) (1997) 265–299.
[48] Y. Ueda, K. Fukuda, Y. Kim, New measuring method of axisymmetric three-dimensional residual stresses using inherent strains as parameters, J. Eng. Mater. Technol. 108 (4) (1986) 328–334.
[49] Y. Ueda, K. Fukuda, K. Nakacho, S. Endo, A new measuring method of residual stresses with the aid of finite element method and reliability of estimated values, Trans. Jpn. Weld. Res. Inst. 4 (2) (1975) 151–157.
[50] K. Zeng, D. Pal, H.J. Gong, N. Patil, B. Stucker, Comparison of 3dsim thermal modelling of selective laser melting using new dynamic meshing method to ansys, Mater. Sci. Technol. 31 (8) (2015) 945–956.